Design of Ordered Mesoporous CeO_2–YSZ Nanocomposite Thin Films with Mixed Ionic/Electronic Conductivity via Surface Engineering

Erdogan Celik,* Pascal Cop, Rajendra S. Negi, Andrey Mazilkin, Yanjiao Ma, Philip Klement, Jörg Schörmann, Sangam Chatterjee, Torsten Brezesinski, and Matthias T. Elm*

ABSTRACT: **Mixed ionic and electronic conductors represent a technologically relevant materials system for electrochemical device applications in the field of energy storage and conversion. Here, we report about the design of mixed conducting nanocomposites by facile surface modification using atomic layer deposition (ALD). ALD is the method of choice, as it allows coating of even complex surfaces. Thermally stable mesoporous thin films of 8 mol % yttria stabilized zirconia (YSZ) with different pore sizes of 17, 24, and 40 nm were prepared through an evaporation induced self assembly process. The free surface of the YSZ films was uniformly coated via ALD with a ceria layer of either 3 or 7 nm thickness. Electrochemical impedance spectroscopy was utilized to probe the influence of the coating on the charge transport properties. Interestingly, the porosity is found to have no effect at all. In contrast, the thickness of the ceria surface layer plays an important role. While the nanocomposites with a 7 nm coating only show ionic conductivity, those with a 3 nm coating exhibit mixed conductivity. The results highlight the possibility of tailoring the electrical transport properties by varying the coating thickness, thereby providing innovative design principles for the next generation electrochemical devices.**

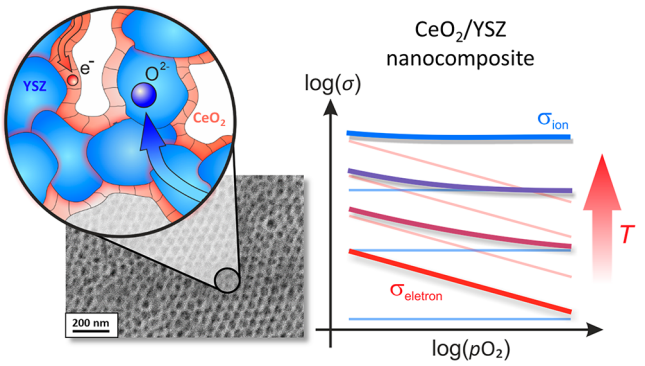

KEYWORDS: *Mesoporous oxides, Nanocomposites, Atomic layer deposition, Surface engineering, Mixed conductors*

Ordered mesoporous metal oxides are characterized by a regular structure made from pores of diameter 2–50 nm.[1,2] The pores are surrounded by crystallites that form an interconnected pathway for electrical charge carriers. The regular pore arrangement enables efficient penetration of gases or liquids into the bulk, thereby improving the accessibility of active surface sites. This characteristic structure qualifies mesoporous oxides for a variety of electrochemical applications,[3−9] e.g., in the field of (photo) electrocatalysis, as electrode materials for batteries and supercapacitors or gas sensors. Several studies have shown that mesoporous architectures are favorable for electro chemical applications, which is mostly attributed to their large specific surface area. However, also other factors, such as the degree of crystallinity, the grain size distribution, and the pore structure, play an important role in outperforming bulk (nanocrystalline) counterparts.[3,10−15]

Surface engineering may lead to further improvements in the properties of mesoporous oxides. The accessibility of the free surface through the porosity enables its effective modifica tion,[16] e.g., by functionalization, deposition of thin coatings, or incorporation of guest species, such as metal nanopar ticles.[17−19] A common approach is surface coating via atomic layer deposition (ALD).[20−22] ALD allows preparing conformal and uniform coatings on complex surfaces, with precise control over their thickness.[22−24] It is therefore often used in surface engineering of nanostructured materials for energy applica

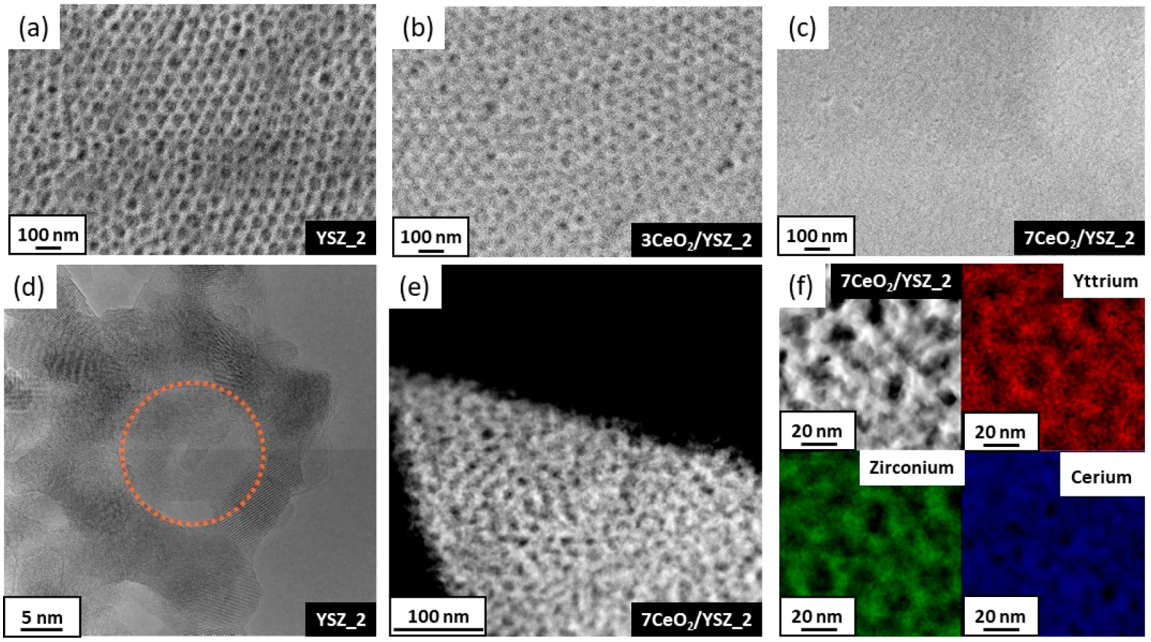

Figure 1. Top view SEM images of (a) uncoated, (b) 3 nm, and (c) 7 nm CeO_2 coated YSZ 2 thin films. (d) HRTEM image of uncoated YSZ 2. (e, f) HAADF STEM images of 7 nm CeO_2 coated YSZ 2 and corresponding EDS maps for Y (in red), Zr (in green), and Ce (in blue).

tions.[22,25−27] One of the benefits of ALD derived thin surface coatings is that the deposition of a simple binary oxide, such as Al_2O_3 or SiO_2, can help increase the thermal stability of mesoporous materials,[28−30] whose structure often tends to collapse at elevated temperatures. Surface modification via ALD is also successfully applied to protect/stabilize cathode materials in lithium ion and solid state batteries[31−37] or to improve the performance of solid oxide fuel cells.[38−40] Apart from that, surface engineering of complex nanostructures using ALD allows developing innovative mixed conducting compo sites. This can be achieved by coating an ion conducting oxide with an electronically conductive material or vice versa. Artificial mixed conductors prepared from two different solid phases represent promising materials systems for various applications, e.g., in the field of energy storage and conversion. They are of importance as intercalation electrodes, permeation membranes, or sensors,[41] as they may exhibit high electronic and ionic partial conductivities. Furthermore, space charge effects at the interface between two different phases can enable interfacial storage of neutral species, such as lithium or silver.[42−44]

Artificial composites are commonly formed by "mixing" an ion conductor with a metal.[45−48] In an alternative approach, mixed conducting properties are achieved by coating the free surface of a porous oxygen ion conductor with thin titania (TiO_2) layers.[49] Mixed conducting properties have also been assumed for mesoporous zirconia (ZrO_2) thin films coated with ceria (CeO_2).[50] However, experimental proof of electronic conductivity of the ceria coating is lacking in the related study, mainly because the oxygen partial pressure dependence of the conductivity has not been examined. Nevertheless, using oxide based coatings as an electronically conductive phase promises higher thermal stability of the resulting composite. In addition, electrochemical character izations revealed that the thickness of the ALD coating has a profound effect on the electrical properties. This is attributed to changes in morphology and microstructure (crystallinity, grain size, etc.) of the coating with varying ALD cycles as well as to space charge effects arising at the different interfaces. The strong correlation between thickness and electrical conductiv ity offers an additional degree of freedom in tailoring the conductivity of mesoporous oxide composites by altering the coating thickness. However, detailed understanding of the relation between coating thickness, morphology, and ionic/electronic conductivity is required to optimize the electro chemical properties for real world (device) applications.

Here, we report about the characterization of mixed conducting nanocomposites by surface engineering of cubic mesoporous yttria stabilized zirconia (YSZ) thin films. YSZ was chosen as a matrix, as it is one of the most prominent oxygen ion conductors at elevated temperatures.[51−53] The high oxygen ion conductivity arises from the incorporation of yttria (Y_2O_3) into the ZrO_2 lattice, stabilizing the cubic fluorite type crystal structure and leading to the formation of oxygen vacancies.[54,55] The free surface of the mesoporous films was coated by ceria ALD. Ceria shows high redox activity of the Ce^{3+}/Ce^{4+} couple, thereby facilitating oxygen exchange with the surrounding atmosphere.[56] In addition, it is responsible for the $p(O_2)$ sensitive mixed ionic/electronic conductivity, as the release of oxygen under reducing conditions not only generates oxygen vacancies but also localized electrons, the latter of which reduce Ce^{4+} to Ce^{3+}:

$$2Ce_{Ce}^{x} + O_{O}^{x} \rightleftharpoons V_{O}^{\cdot\cdot} + 2Ce_{Ce}^{\prime} + \frac{1}{2}O_2 \quad (1)$$

These electrons can hop as small polarons between the Ce^{3+} and Ce^{4+} sites, giving rise to an electronic conductivity contribution.[57−59] Thus, the electrical properties of $CeO_{2-\delta}$ strongly vary with the nonstoichiometry δ.[60,61]

Specifically, polymer templated, mesoporous CeO_2−YSZ nanocomposite thin films with different pore sizes and varying thicknesses of the ceria coating are examined. Structural characterization confirms the uniform coating of the free surface via ALD. Temperature and oxygen partial pressure

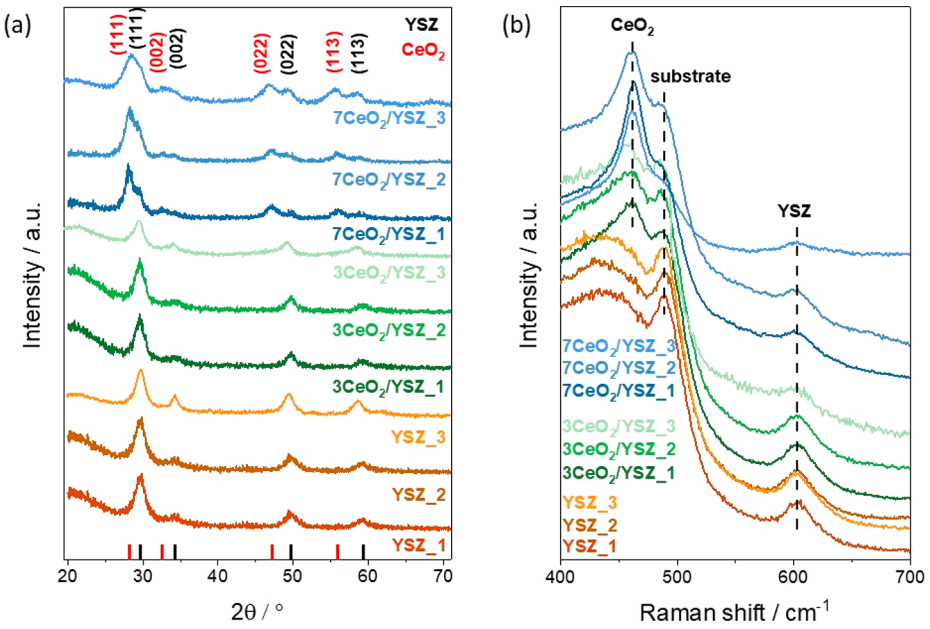

Figure 2. (a) GIXRD patterns and (b) Raman spectra of uncoated and CeO_2 coated YSZ thin films at room temperature. For comparison, the reference patterns for cubic YSZ (PDF 98 007 5316) and cubic CeO_2 (PDF 98 002 8709) are shown in part a.

dependent electrochemical impedance spectroscopy (EIS) measurements indicate that the electrical transport properties are independent of the pore size but strongly change with the thickness of the coating. Mixed ionic/electronic conductivity arises when the surface is coated with a 3 nm ceria layer, as clearly confirmed by $p(O_2)$ dependent conductivity measurements. The electronic partial conductivity of the ceria layer dominates the transport properties at low temperatures and under reducing conditions. In contrast, nanocomposites with a 7 nm ceria coating only show ionic conductivity. The results demonstrate that surface modification of mesoporous oxides is a viable approach to produce and explore mixed conducting materials systems with tailorable properties.

RESULTS AND DISCUSSION

Structural and Compositional Characterization. Representative top view SEM images of uncoated mesoporous YSZ thin films (thickness $d \simeq 180$ nm) are shown in Figure 1a and Figure S1. The pores have average in plane diameters of 17, 24, and 40 nm. In the following, the corresponding films are referred to as YSZ 1, YSZ 2, and YSZ 3, respectively. Both YSZ 1 and YSZ 2 are crack free and have a continuous pore structure with a distorted cubic symmetry. The high resolution TEM (HRTEM) images in Figure 1d and Figure S2 confirm that the pores (denoted by an orange circle) are surrounded by crystalline walls having grains of average diameter 5 nm, independent of the pore size. As opposed to YSZ 1 and YSZ 2, YSZ 3 shows a disordered but macroscopically uniform porous network (see Figure S1), a result that we attribute to the lower solubility of the high molecular weight structure directing agent (SDA) used in the synthesis.

For the preparation of nanocomposites, the different thin films were coated via ALD with a ceria layer of either 3 nm ($3CeO_2$/YSZ x) or 7 nm ($7CeO_2$/YSZ x) thickness. After surface coating, they were probed using SEM, mainly focusing on the change in pore size with the number of ALD cycles. As shown in Figure 1b,c and Figure S2 for YSZ 2, the pores shrink significantly with increasing ALD cycles. For $7CeO_2$/YSZ 1, the pores were virtually completely filled (Figure S1). Also for YSZ 2 (Figure 1c), the pores appeared to be largely filled after coating with 7 nm ceria. However, STEM images of the corresponding $7CeO_2$/YSZ 2 nanocomposite (Figure 1e,f and Figure S2) demonstrate that some of the porosity is maintained. This is further supported by energy dispersive X ray spectroscopy (EDS) maps of the elemental distribution for the $3CeO_2$/YSZ 2 and $7CeO_2$/YSZ 2 thin films in Figure 1f and Figure S2. The mapping of Ce reveals a uniform coating distribution, suggesting good surface coverage of the YSZ matrix.

The crystallinity and phase purity of the nanocomposites were investigated by GIXRD at room temperature. Figure 2a presents GIXRD patterns for all samples. The uncoated YSZ films show characteristic reflections of cubic YSZ, indicating successful preparation of a single phase material.[62] Applying the Scherrer equation to the (111) reflection, a crystallite size of approximately 6 nm was calculated, in good agreement with the value estimated from TEM imaging.[63] After ALD coating, additional broad reflections are visible in the diffraction patterns. These reflections can be assigned to the cubic fluorite structure of CeO_2. They sharpen and increase in intensity for the films coated with a 7 nm ceria layer, which is in line with previous results.[50] However, for YSZ and ceria, the low scattering factor of oxygen and the broad reflections, due to the small crystallite size, make a clear differentiation between the cubic and tetragonal phases difficult.[64−66]

Raman spectroscopy measurements were conducted to confirm the cubic lattice symmetry of both the mesoporous YSZ and the ceria coating. As shown in Figure 2b, Raman spectra of the uncoated YSZ films display the characteristic triply degenerate F_{2g} mode at 604 cm^{-1}, which is typical of the cubic fluorite phase.[54,67,68] Note that the intense mode at 490 cm^{-1} and the broad Raman band at 430 cm^{-1} arise from the quartz glass substrate.[69] For the CeO_2−YSZ nanocomposites, the Raman measurements also confirm the fluorite crystal structure of ceria, due to the presence of the prominent Raman active band at $\omega = 461$ cm^{-1}. The samples show a red

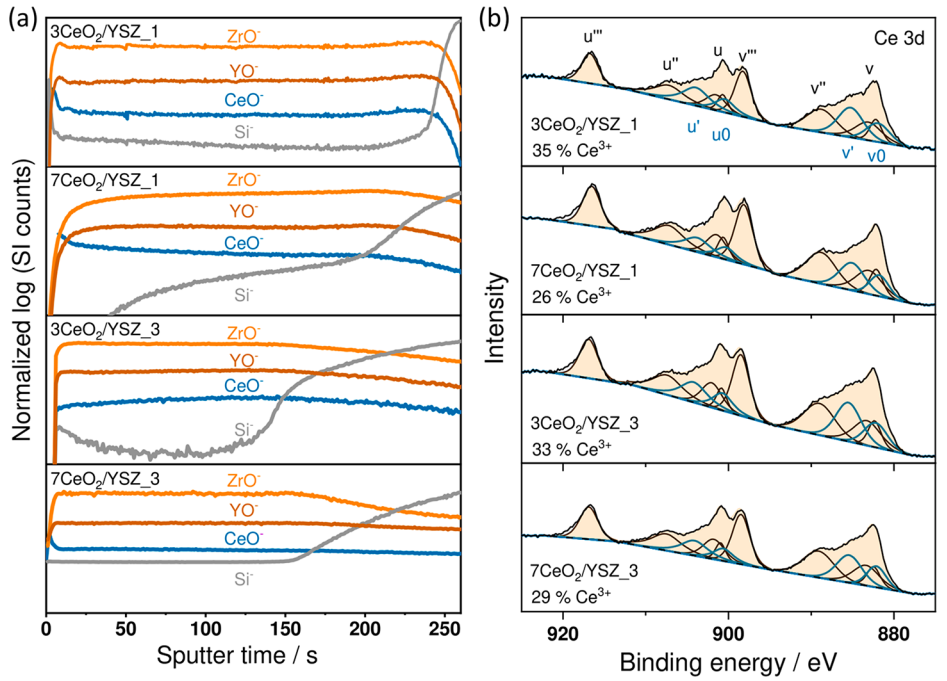

Figure 3. (a) ToF SIMS depth profiles for 3 and 7 nm CeO_2 coated YSZ 1 and YSZ 3 thin films and (b) corresponding Ce 3d XP spectra.

shift and broadening of the F_{2g} mode, compared to single crystals (ω = 465 cm^{-1}),[70,71] both of which slightly increase with decreasing coating thickness. This behavior is characteristic of nanoscale ceria[72−77] and indicates its columnar growth on the YSZ surface.[23] Phonon confinement and changes in the lattice constant (tensile strain) result in broadening of the Raman mode and a shift to lower wavenumbers with decreasing particle size. Thus, the red shift of the F_{2g} mode observed for decreasing coating thickness suggests a smaller grain size for the 3 nm CeO_2. However, strain effects arising at the CeO_2/YSZ interface may be responsible for the broadening and shift of the F_{2g} mode too.[78]

The homogeneity of the CeO_2 coating throughout the films was examined by time of flight secondary ion mass spectrometry (ToF SIMS). Figure 3a shows depth profiles for YSZ 1 and YSZ 3 after the deposition of 3 and 7 nm CeO_2. For all samples, a constant ratio of YO^- and ZrO^- species (until reaching the film/substrate interface) is found, indicating uniform distribution of Y and Zr throughout the mesoporous films. In addition, the CeO^- signal clearly follows that of YO^- and ZrO^-, confirming the conformal coating of the inner (bulk) porosity. The slight decrease/increase of the CeO^- signal with increasing sputtering depth seen for $7CeO_2$/YSZ 1 and $3CeO_2$/YSZ 3 is related to the porous structure of the nanocomposites, as discussed previously.[23] Interestingly, no SiO^- signal is detected for the $7CeO_2$/YSZ 1 at short sputtering times. This result suggests complete coverage of the top surface, as also indicated by SEM imaging in Figure S1. This was somewhat expected though, as in that case, the pore radius is similar to the thickness of the ALD ceria layer. Note that blocking of the interconnecting channels (necks) between the pores prevents proper filling and results in growth of a sealing layer.[21,50,79] However, a nearly constant CeO^- signal is found after a short sputtering time, accompanied by the presence of the Si^- substrate signal, thereby corroborating the uniform coverage of the solid/air interfaces in the YSZ 1 thin film.

It is well known that the mixed conducting properties of ceria are strongly correlated with its ability to switch between the +3 and +4 oxidation states.[57,58,61] For that reason, the CeO_2/YSZ nanocomposites were investigated by XPS to determine the Ce^{3+} content in the surface coating. To calculate the Ce^{3+} content, the integral areas of the six signals from Ce^{4+} (v, v'', v''' and u, u'', u''') and the four signals from Ce^{3+} (v_0, v' and u_0, u') were compared.[80] Figure 3b shows Ce 3d XP spectra and corresponding fits for the 3 and 7 nm CeO_2 coated YSZ 1 and YSZ 3 thin films. The analysis reveals that the Ce^{3+}/Ce^{4+} ratio is independent of the pore size but varies with the coating thickness. With increasing thickness of the CeO_2 layer, the Ce^{3+} concentration decreases, in good agreement with previous data[50] and the results from Artiglia et al.[81] Despite the different pore structures and surface areas (for the CeO_2 to be deposited onto), only small differences in the Ce^{3+} content between the $3CeO_2$/YSZ 1 (35%) and $3CeO_2$/YSZ 3 (33%), as well as between the $7CeO_2$/YSZ 1 (26%) and $7CeO_2$/YSZ 3 (29%), are observed. Thus, the difference clearly derives from the thickness of the coating in the nanocomposites. Typically, the nonstoichiometry of $CeO_{2-\delta}$, and therefore the Ce^{3+} content, is determined by the surrounding atmosphere (refer to eq 1). However, because the XPS measurements were performed under identical conditions, the decrease in Ce^{3+} signal with increasing coating thickness suggests the presence of a surface space charge region (where the electrons accumulate).[3,54,82] Since XPS is a surface sensitive technique with a typical penetration depth of approximately 5 nm,[32] the width of the space charge layer can be considered to be confined to only a few nanometers. Note that a high surface concentration of Ce^{3+} has also been reported by Hao et al. They monitored the Ce^{3+} distribution in ceria nanoparticles using scanning tunneling microscopy (STM) combined with electron energy loss spectroscopy (EELS).[83]

Electrochemical Characterization. The electrochemical properties of the uncoated YSZ films and corresponding

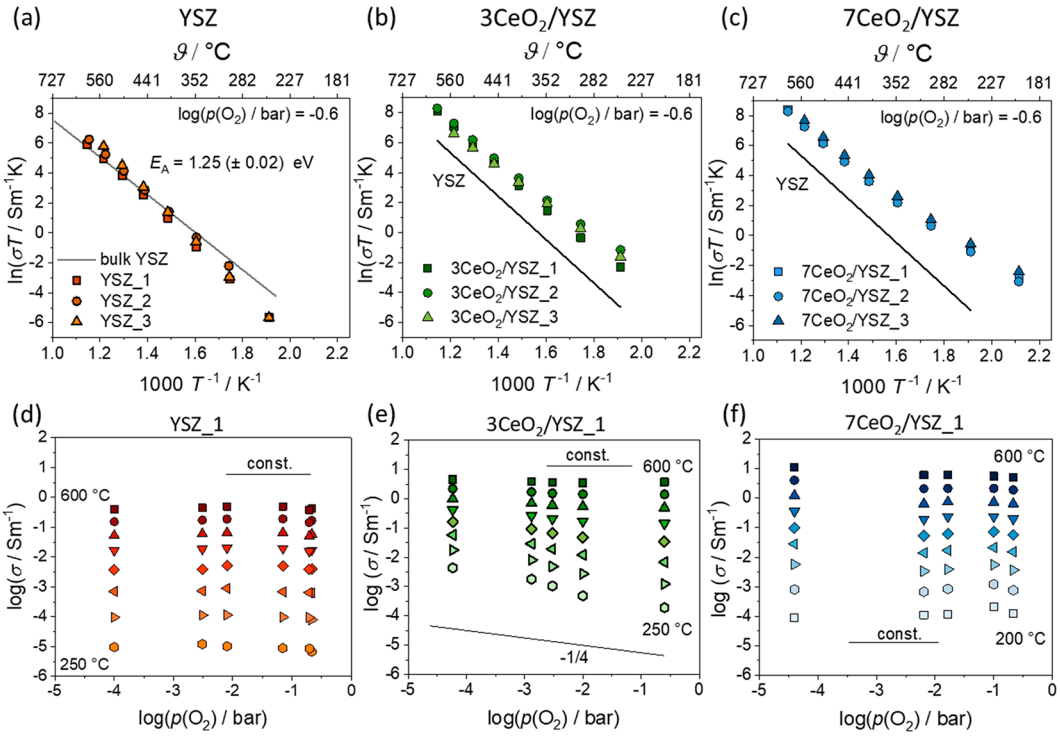

Figure 4. Arrhenius plots of the total conductivity for (a) uncoated, (b) 3 nm, and (c) 7 nm CeO_2 coated YSZ thin films. The gray line in part a is the average of reported values for bulk YSZ taken from ref 91. Oxygen partial pressure dependence of the total conductivity for (d) uncoated, (e) 3 nm, and (f) 7 nm CeO_2 coated YSZ 1.

nanocomposites were studied as a function of temperature between 200 and 600 °C in 50 °C steps and oxygen partial pressure (approximately 10^{-5} and 0.2 bar) using electro chemical impedance spectroscopy (EIS). Representative impedance spectra (Nyquist plots) recorded at 450 °C are shown in Figure S3. Figure S4 shows the impedance spectra for the $7CeO_2$/YSZ 1 measured at different temperatures (200–600 °C). All spectra exhibit an almost ideal semicircle at high frequencies, as commonly observed for mesoporous metal oxide thin films.[54,84] At low frequencies, the appearance of a second semicircle is apparent. Consequently, the EIS data were fitted using an equivalent circuit with two *RQ* elements connected in series. The elements represent one of the two semicircles and consist of a resistance element *R* and a constant phase element *Q* connected in parallel. The capacitance values were calculated from the parameters α and C_Q of the constant phase element according to[85,86]

$$C = R^{(1-\alpha)}C_Q^{(1/\alpha)} \tag{2}$$

For the semicircle at high frequencies, capacitances of 1.6–4.3 × 10^{-12} F were obtained. Typical values for the bulk of ceramic materials vary between 10^{-12} and 10^{-10} F.[87,88] Thus, the first semicircle is attributed to the response of the nanocomposite. At low frequencies, the tail of the second semicircle can be described by a capacitance of approximately 10^{-7} F, which corresponds to the contribution of the nanocomposite/electrode interface.[87,88] It is worth noting that in microcrystalline materials, a third semicircle in the intermediate frequency range arises, due to the transport across the grain boundaries. However, in nanocrystalline samples, the semicircles representing the grain and grain boundary contributions merge, making a separation impossible.[3,61,89] For that reason, only the total resistance (i.e., grain and grain boundary) is obtained from the analysis of the high frequency semicircle. The total conductivity σ_{tot} was determined from the resistance *R* and the geometry of the interdigitated electrodes used for the electrical characterization:[90]

$$\sigma_{tot} = \frac{1}{R}\cdot\frac{b}{dl_{finger}n} \tag{3}$$

where b = 33 μm is the distance between the electrode fingers, n = 20 the number of fingers, l_{finger} = 3 mm the length of an electrode finger, and d = 180 nm represents the film thickness (see also Figure S5). Using eq 3, the porosity is neglected, meaning the samples are treated as being dense.

Figure 4a shows the temperature dependence of the conductivity for the uncoated YSZ films in an Arrhenius type representation. The same conductivity was found for YSZ 1, YSZ 2, and YSZ 3. This is somewhat surprising, as the microstructure can significantly affect the impedance of polycrystalline ceramics.[86,92,93] The pore size independent conductivity can probably be attributed to the characteristic architecture of the mesoporous YSZ thin films. Despite differences in the average pore size, they all exhibit a regular arrangement of crystallites of very similar size, giving rise to comparable transport pathways for the charge carriers. As is evident from the data, the samples showed a linear Arrhenius behavior over the whole temperature range investigated. This is expected, as YSZ exhibits ionic conductivity because of the presence of oxygen vacancies resulting from the introduction of yttria into the zirconia lattice. This kind of substitution can be described in Kroeger–Vink notation by:[55]

$$Y_2O_3 \xrightarrow{ZrO_2} 2Y'_{Zr} + V^{\cdot\cdot}_O + 3O^x_O \tag{4}$$

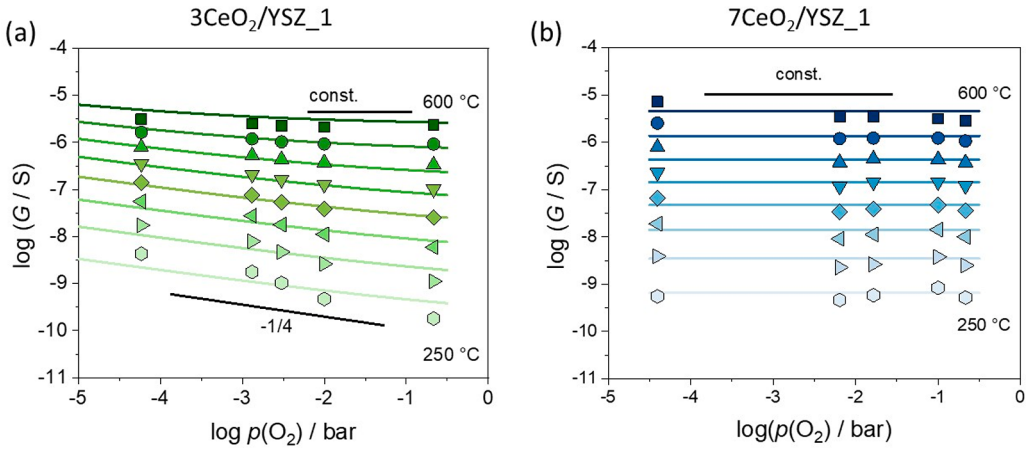

Figure 5. Calculated oxygen partial pressure dependence of the conductance for (a) 3 nm and (b) 7 nm CeO_2 coated YSZ 1 thin films. Solid lines are fits to the experimental data.

where Y'_{Zr} represents a Y^{3+} ion on a Zr^{4+} site with a relative charge of −1, and $V_O^{\cdot\cdot}$ is an oxygen vacancy with a relative charge of +2. O_O^x denotes the oxygen lattice sites with a relative charge of zero. From the temperature dependence of the conductivity, the activation energy E_A and the pre exponential conductivity factor σ_0 were derived:

$$\sigma_{ion}(T) = \frac{\sigma_{0,ion}}{T} \exp\left(-\frac{E_A}{k_B T}\right) \quad (5)$$

where k_B is the Boltzmann constant, $\sigma_{0,ion}$ the conductivity prefactor, and T represents the temperature. For the uncoated YSZ samples, an activation energy $E_{A,ion}$ = 1.25 (±0.02) eV was obtained. This is in good agreement with the values reported for oxygen ion conductivity in nanocrystalline YSZ, ranging from 1.02 to 1.23 eV.[49,54,88,91] Also, the measured conductivities are similar to the average of reported values for bulk YSZ taken from ref 91 (shown as a solid gray line in Figure 4a). A dominant oxygen ion conductivity is also confirmed by the $p(O_2)$ independent conductivity shown in Figure 4d.[55] As the concentration of oxygen ions is fixed for varying $p(O_2)$, due to the "doping" with yttria, the activation energy represents the migration enthalpy ΔH_{mig} of the oxygen ions. For the conductivity prefactor $\sigma_{0,ion}$, a value of 7.5 (±0.3) × 10^9 $Sm^{-1}K$ was obtained.

Coating the mesoporous YSZ films significantly changes their electrical properties. After the deposition of 3 nm ceria, the total conductivity of the nanocomposites increases by at least 2 orders of magnitude compared to that of the pristine YSZ material (Figure 4b). Two transport regimes with different activation energies can be observed at ambient conditions in the Arrhenius representation. The change in activation energy becomes even more evident when calculating the activation energy as a function of the inverse temperature:

$$E_A = -k_B \frac{d(\ln(\sigma T))}{d(1/T)} \quad (6)$$

As shown in Figure S6, the activation energy clearly decreases with decreasing temperature. In addition, the CeO_2 coating affects the $p(O_2)$ dependence of the conductivity in the temperature range between 250 and 600 °C, as shown in Figure 4e. At lower temperatures, the conductivity varies with a characteristic slope of −1/4, while at higher temperatures, it remains constant in the $p(O_2)$ range investigated.

The 7CeO_2/YSZ nanocomposites show the highest total conductivity at all temperatures (Figure 4c). Again, two different transport regimes characterized by changes in activation energy are observed (see also Figure S6). However, in contrast to the 3CeO_2/YSZ samples, the 7CeO_2/YSZ nanocomposites reveal a constant $p(O_2)$ dependence of the conductivity at all temperatures (Figure 4f). Similar to the uncoated YSZ films, the effect of pore size on the transport properties is negligible. Instead, the thickness of the CeO_2 layer determines the differences in conductivity seen.

Direct comparison of the conductivity is somewhat questionable when analyzing the influence of the coating on the electrical properties of the nanocomposites, because the deposition of the surface layer decreases the pore size, which was neglected in the calculation, as discussed previously. It is more reasonable to compare the total conductance $G = R^{-1}$, comprising the ionic conductance G_{YSZ} of the mesoporous YSZ matrix and the conductance G_{CeO_2} of the ceria coating. The transport through the coating occurs in parallel to the transport of the oxygen ions in the YSZ, i.e., the total conductance is given by $G_{total} = G_{YSZ} + G_{CeO_2}$. The contribution of the CeO_2 layer was determined from the total conductance of the nanocomposites by subtracting the conductance of the mesoporous YSZ films ($G_{CeO_2} = G_{total} - G_{YSZ}$). This is possible because the YSZ samples exhibit the same conductivity (independent of pore size, see above). The resulting $p(O_2)$ dependence of the individual conductance contributions from the 3 and 7 nm ceria coatings are shown in Figure 5a,b.

The 7 nm CeO_2 coating shows a $p(O_2)$ independent conductivity over the whole temperature and oxygen partial pressure range (Figure 5b). This behavior suggests that the surface layer exhibits a dominant oxygen ion conductivity, as ceria tends to form intrinsic anti Frenkel defect pairs.[57] We attribute the two transport regimes with different activation energies to the presence of a small amount of acceptor impurities (A) in the coating. The formation of oxygen vacancies, due to acceptor impurities, is given in Kroeger−Vink notation by:[94]

$$A_2O_3 \xrightarrow{CeO_2} 2A'_{Ce} + V_O^{\cdot\cdot} + 3O_O^x \quad (7)$$

At low temperatures, the presence of these impurities leads to a constant oxygen vacancy concentration $[V_O^{\cdot\cdot}]_A$, which is significantly larger than the intrinsic one due to anti Frenkel defects, i.e., $[V_O^{\cdot\cdot}]_A \gg [V_O^{\cdot\cdot}]_{AF}$. The temperature dependence of the conductivity is then only determined by the migration enthalpy $\Delta_{mig}H_{ion}$ of the oxygen vacancies:

$$\sigma_{ion,Imp}(T) = Zne\mu(T) \approx 2[V_O^{\cdot\cdot}]_A F\frac{\mu_0}{T}\exp\left(-\frac{\Delta_{mig}H_{ion}}{k_BT}\right) \tag{8}$$

where $[V_O^{\cdot\cdot}]_A = n/N_A$ is the oxygen vacancy concentration (due to acceptor impurities), n the corresponding density of oxygen vacancies, N_A the Avogadro constant, e the elementary charge, F the Faraday constant, Z the valence, and μ_0 represents the mobility prefactor. Hence, the low temperature activation energy $E_{A,Imp}$ corresponds to the migration enthalpy of the oxygen ions:

$$E_{A,Imp} = \Delta_{mig}H_{ion} \tag{9}$$

At higher temperatures, intrinsic anti Frenkel defects are prevalent, leading to the formation of oxygen vacancies $V_O^{\cdot\cdot}$ and oxygen interstitials O_i'':

$$CeO_2 \rightarrow Ce_{Ce}^{x} + 2V_O^{\cdot\cdot} + 2O_i'' \tag{10}$$

Consequently, the concentration of the intrinsic oxygen vacancies increases and outweighs the constant vacancy concentration, due to the presence of acceptor defects. The ionic conductivity in the high temperature region is therefore given by

$$\sigma_{ion,AF}(T) = Zn(T)e\mu(T) \approx 2[V_O^{\cdot\cdot}]_{AF}F\frac{\mu_0}{T}\exp\left(-\frac{\Delta_{mig}H_{ion}}{k_BT}\right)\exp\left(-\frac{\Delta_fH_{ion}}{2k_BT}\right) \tag{11}$$

where $n(T)/N_A \approx [V_O^{\cdot\cdot}]_A F\exp(-\Delta_fH_{ion}/2k_BT)$ is the concentration of the intrinsic oxygen vacancies (due to anti Frenkel defects). In this case, the activation energy of the ionic conductivity $E_{A,AF}$ comprises the $\Delta_{mig}H_{ion}$ and the enthalpy of formation Δ_fH_{ion} of the anti Frenkel defects:

$$E_{A,AF} = \Delta_{mig}H_{ion} + \frac{\Delta_fH_{ion}}{2} \tag{12}$$

The temperature dependence of the ionic conductance of the ceria coating is then given by

$$G_{ion,CeO_2}(T) = G_{ion,Imp}(T) + G_{ion,AF}(T) \tag{13}$$

with

$$G_{ion,Imp}(T) = \frac{G_{0,Imp}}{T}\exp\left(-\frac{E_{A,Imp}}{k_BT}\right) \tag{14}$$

and

$$G_{ion,AF}(T) = \frac{G_{0,AF}}{T}\exp\left(-\frac{E_{A,AF}}{k_BT}\right) \tag{15}$$

A good description of the experimental results (see solid line fits in Figure 5b) is achieved for $E_{A,Imp} = \Delta_{mig}H_{ion} = 0.91$ ($\pm$0.03) eV and $E_{A,AF} = 1.96$ ($\pm$0.02) eV and the conductance prefactors $G_{0,Imp} = 200$ ($\pm$12) SK and $G_{0,AF} = 5.9$ ($\pm$1.0) $\times 10^8$ SK. The activation energies are in excellent agreement with previous studies.[94,95] From eq 12, the Δ_fH_{ion} is calculated to be approximately 2.1 eV, which is also consistent with literature values.[96−98]

In case of the 3 nm CeO_2 coating (Figure 5a), the conductance decreases with increasing oxygen partial pressure, which is typical of CeO_2 with a dominant electronic conductance. In the near stoichiometric $p(O_2)$ range (intrinsic regime), a decrease in oxygen partial pressure results in the release of molecular oxygen (reduction reaction) according to eq 1. As the concentration of oxygen vacancies is much larger than that of the electrons, the vacancy concentration can be assumed constant (Brouwer approximation). Then, the electron concentration, and therefore the conductance, varies with $p(O_2)^{-1/4}$, in agreement with the experimental results.[3,57,61,84,99] However, at higher temperatures, the conductance again becomes $p(O_2)$ independent, indicating a dominant ionic conductivity, as observed for the $7CeO_2$/YSZ thin films. Thus, the results provide clear evidence that the $3CeO_2$/YSZ nanocomposites exhibit a mixed ionic/electronic conductance:

$$G_{tot,CeO_2}(T, p(O_2)) = G_{ion,CeO_2}(T) + G_{elec}(T, p(O_2)) \tag{16}$$

Like for the 7 nm coating, the ionic conductance of the nanocrystalline CeO_2 surface layer is described by eq 13. The additional electronic contribution, due to hopping of electrons between the Ce^{3+} and Ce^{4+} sites, is given by[60,100,101]

$$G_{elec}(T, p(O_2)) = \frac{G'_{0,elec}}{T}\exp\left(-\frac{E_{A,elec}}{k_BT}\right)\cdot p(O_2)^{-1/4} \tag{17}$$

The corresponding fits of the temperature and $p(O_2)$ dependences of the total conductivity are shown in Figure 5a. Fits to the experimental data for the 3 and 7 nm CeO_2 coated YSZ 2 and YSZ 3 thin films are presented in Figure S7, while in Figure S8, the electronic and ionic contributions to the total conductance are displayed separately. A good data description is achieved for $E_{A,Imp} = 0.93$ ($\pm$0.03) eV and $E_{A,AF} = 1.94$ ($\pm$0.02) eV, in agreement with the results for the $7CeO_2$/YSZ nanocomposite. The prefactors $G_{0,Imp} = 66.7$ ($\pm$12.0) SK and $G_{0,AF} = 2.8$ ($\pm$0.3) $\times 10^8$ SK are reduced by a factor of 3 and 2.1, respectively (see also Table S1), corresponding to the difference in thickness of the coatings. Overall, the results indicate that both the 3 and 7 nm CeO_2 surface layers exhibit a comparable ionic conductivity. For the electronic conductance, an activation energy $E_{A,elec} = 0.86$ ($\pm$0.02) eV and a conductance prefactor $G'_{0,elec} = 18.2$ ($\pm$1.0) SK bar$^{1/4}$ are obtained. In the intrinsic regime, the activation energy again comprises the migration enthalpy $\Delta_{mig}H_{elec}$ and the enthalpy of formation Δ_fH_{elec} of the electronic defects:[61,99,102,103]

$$E_{A,elec} = \Delta_{mig}H_{elec} + \frac{\Delta_fH_{elec}}{2} \tag{18}$$

A typical value of 0.4 eV for $\Delta_{mig}H_{elec}$ has been reported for a small polaron hopping in ceria.[50,59,60,102] Using this, Δ_fH_{elec} is calculated to be approximately 0.92 eV, which is significantly lower than for single crystals (4.2−4.7 eV).[59,61] However, comparable values have been reported for nanocrystalline ceria.[61] The decrease in Δ_fH_{elec} originates from the space charge potential at the grain boundaries. As shown by Tschöpe et al. using the space charge model, the apparent activation energy of the electrons decreases from 2.7 eV to approximately 1.0 eV when decreasing the grain size to 30 nm. In addition,

calculations using density functional theory (DFT) predict that the high surface area of ceria nanoparticles strongly affects $\Delta_f H_{elec}$ and facilitates oxygen release.[104,105] The low reduction enthalpy further confirms that space charge effects are responsible for the high Ce^{3+} concentration in the 3 nm coating.

The increased electronic conductivity of the $3CeO_2$/YSZ nanocomposites can directly be related to the higher Ce^{3+} concentration, as observed by XPS (see Figure 3b). Because the electrons can only move as small polarons between the Ce^{3+} and Ce^{4+}, the conductivity prefactor depends on the number of available hopping sites in the lattice:[57,58]

$$\sigma_{elec}(T, p(O_2)) = \frac{n_{Ce} x_{Ce^{3+}}(1 - x_{Ce^{3+}}) e^2 a^2 \nu_0}{k_B T} \exp\left(-\frac{E_{A,elec}}{k_B T}\right) \quad (19)$$

Here, n_{Ce} is the number of Ce lattice sites per unit volume, $x_{Ce^{3+}}$ the fraction of Ce^{3+} ions, which is dependent on the oxygen partial pressure of the surrounding atmosphere, e the elementary charge, a the distance between the hopping sites, i.e., the lattice constant, and ν_0 represents the attempt frequency for the jump process. In addition, a high nonstoichiometry increases the lattice constant a (chemical strain effect), due to the larger ionic radius of Ce^{3+} compared to Ce^{4+},[106] which further increases the conductivity prefactor. This assumption is supported by the Raman data shown in Figure 2b, where the red shift and broadening of the F_{2g} mode are related to tensile strain in the coating.

CONCLUSIONS

In this work, we have successfully synthesized polymer templated, cubic mesoporous YSZ thin films with different pore sizes. The free surface of the YSZ matrix was coated with a CeO_2 layer of defined thickness using ALD to produce mixed conducting nanocomposites. Structural characterization confirmed the single phase nature and uniformity of the nanocrystalline YSZ (framework) and CeO_2 (coating) materials. Electrochemical impedance spectroscopy measure ments were conducted on the samples at different temper atures and oxygen partial pressures to examine the effect that the coating thickness has on the transport properties. Our study indicates that the thickness of the CeO_2 coating affects the total conductivity because of changes in the Ce^{3+}/Ce^{4+} ratio and microstructure properties of the surface layer. For 3 nm coating, the total conductivity exhibits an additional electronic contribution. In contrast, nanocomposite thin films with a 7 nm coating only show oxygen ion conductivity over the whole temperature and oxygen partial pressure ranges investigated. The results emphasize that surface engineering of mesoporous metal oxides via ALD holds great potential for the development of nanocomposites, whose electrical properties can be tailored by varying the coating thickness. Overall, this approach offers promising possibilities for the synthesis of mixed conductors with optimized transport properties for electrochemical applications.

METHODS AND EXPERIMENTAL DETAILS

Materials. $YCl_3 \cdot 6H_2O$, $ZrCl_4$, glacial acetic acid, absolute ethanol, 2 methoxyethanol, and tetrahydrofuran were purchased in the highest available purity from Sigma Aldrich and used as received. $H[C(CH_3)_2CH_2]_x C_6H_4(OCH_2CH_2)_y OH$ (PIB_x *b* PEO_y) diblock copoly mers with $x = 53/y = 45$, $x = 107/y = 150$, and $x = 357/y = 454$, referred to as PIB_{53} *b* PEO_{45}, PIB_{107} *b* PEO_{150}, and PIB_{357} *b* PEO_{454},[107−110] respectively, served as structure directing agents (SDAs).

Synthesis. Ordered mesoporous YSZ thin films were prepared by the dip coating method on quartz glass substrates using an evaporation induced self assembly (EISA) process.[54,111,112] The dip coating solutions consisted of 40 mg of SDA, 35.9 mg of $YCl_3 \cdot 6H_2O$, and 145 mg of $ZrCl_4$ dissolved in a mixed solvent of glacial acetic acid, absolute ethanol (or tetrahydrofuran), and 2 methoxyethanol (see summary in Table S2, Supporting Information, for more details). The withdrawal rate was set to 5−15 mm/s. During the film formation process, the relative humidity was controlled in the range between 15 and 25%. The as made samples were transferred to an oven for drying at 120 °C for 1 h. Subsequently, they were heated to 300 °C at 5 °C/min with 12 h dwell time to stabilize the mesostructure. Crystallization and SDA removal were achieved by heating to 600 °C at 5 °C/min with 1 h dwell time.

Atomic Layer Deposition. CeO_2 was deposited onto the surface of the mesoporous YSZ films at a temperature of 250 °C using a commercial ALD system (PicoSun R200 Standard). For the deposition, the cerium precursor, tetrakis(2,2,6,6 tetramethyl 3,5 heptanedionato)cerium(IV) (97%, abcr GmbH), referred to as $Ce(TMHD)_4$, was heated to 195 °C and the corresponding valve block connected to the reaction chamber kept at 230 °C. For a single ALD cycle, a 2 s pulse $Ce(TMHD)_4$ with 150 sccm nitrogen carrier gas was followed by a 60 s nitrogen purging step. Next, ozone, generated by an AC 2025 ozone generator 2000 from Teledyne API, was pulsed for 2 s. The ALD cycle was completed by an additional nitrogen purge pulse of 60 s. Under these conditions, the growth rate of CeO_2 is 0.3 Å per cycle, as discussed in more detail elsewhere.[50] The YSZ films were coated using 80 and 190 cycles, resulting in CeO_2 thicknesses of around 3 and 7 nm, respectively.

Structural Characterization. The crystallinity was investigated by grazing incidence X ray diffraction (GIXRD) on a PANalytical X'Pert^3 MRD diffractometer using an incidence angle of $\omega = 0.25°$ and a 2θ scanning range of 20−70°. The scan speed was set to 0.6° min^{-1}, and the step size was 0.01°. Raman measurements were carried out using an inVia Raman microscope from Renishaw in back scattering geometry with an excitation wavelength of $\lambda = 633$ nm. Scanning electron microscopy (SEM) images were recorded on a MERLIN from Carl Zeiss at 3 kV. Transmission electron microscopy (TEM) was performed on a Themis Z (ThermoFisher Scientific) double corrected transmission electron microscope operated at 300 kV. Pieces of the samples were placed on Quantifoil Cu grids with a carbon film of thickness 2 nm. Scanning TEM (STEM) images were recorded using a high angle annular dark field (HAADF) detector. Elemental maps were acquired using a Super X EDS (EDAX) detector. X ray photoelectron spectroscopy (XPS) measurements were performed with a PHI 5000 VersaProbe II from Ulvac Phi using Al−Kα radiation ($\lambda = 1486.6$ eV). A spot of diameter 200 μm was measured utilizing 50 W, 0.5 kV, and 20 ms per step. A pass energy of 23.5 eV was applied for the survey spectra, while 117.4 eV was applied for the detailed spectra of Ce 3d, Y 3d, and Zr 3d. The spectra were calibrated by setting the C 1s peak at 284.8 eV. The software CasaXPS V2.3.17 was used for peak analysis. In addition to the six signals from CeO_2 (v, v'', v''' and u, u'', u'''), four signals from Ce_2O_3 (v_0, v' and u_0, u') were considered,[113] the latter of which typically arise because of the presence of Ce^{3+} at the interface.[23,50] In order to achieve better results, a combination of two signals for fitting the asymmetry (u and v) was used, in agreement with the findings of Skála et al.[114] Time of flight secondary ion mass spectrometry (ToF SIMS) was performed using a ToF.SIMS 5 10 instrument from IONTOF GmbH (Muenster, Germany) equipped with at 25 keV Bi cluster primary ion gun. Depth profiling was done using Cs^+ ions at 1 keV and 50 nA, generating a 100 × 100 μm^2 crater. A 50 × 50 μm^2 of the crater was analyzed with a resolution of 256 × 256 $pixel^2$ using a Bi(I) primary ion source, collecting only the negatively charged ions. Data evaluation was done with the software SurfaceLab7.0 from IONTOF GmbH.

Preparation of Microelectrodes. Interdigitated Pt micro electrodes on the top surface of the films were produced by

photolithography. To this end, a positive photoresist was used (ma P 1215, micro resist technology GmbH). For metallization, Pt was deposited by pulsed laser deposition (PLD) using a KrF excimer laser with a wavelength of λ = 248 nm. The interdigitated Pt electrodes had a thickness of around 200 nm and were made of 20 fingers of 3 mm length and 47 μm width. The distance between the fingers was 33 μm. The Pt electrode configuration is schematically shown in Figure S5 of the Supporting Information.

Electrochemical Characterization. The electrochemical properties of the YSZ thin films were investigated by electrochemical impedance spectroscopy (EIS) in the frequency range between 1 mHz and 10 MHz using a Novocontrol Alpha A impedance bridge. The voltage amplitude was 100 mV. The temperature was varied between 200 and 600 °C. The oxygen partial pressure was controlled in the range of $-5 < \log(p(O_2)/\text{bar}) < 0$ using gas mixtures of argon and oxygen. EIS data were evaluated by means of the software RelaxIS 3.[49]

ASSOCIATED CONTENT

Supporting Information

The Supporting Information is available free of charge at https://pubs.acs.org/doi/10.1021/acsnano.1c11032.

Top view SEM images of the investigated thin films; HRTEM images of uncoated YSZ; HAADF STEM images and EDS maps of ceria coated YSZ; impedance spectra of uncoated and ceria coated YSZ; schematic illustration of the interdigitated Pt electrodes; activation energy as a function of temperature for uncoated and ceria coated YSZ; oxygen partial pressure dependence of the total conductivity; Arrhenius plots of the total conductance and fitting parameters of the transport properties for ceria coated YSZ; and recipes for the synthesis of mesoporous 8YSZ thin films (PDF)

AUTHOR INFORMATION

Corresponding Authors

Erdogan Celik − *Center for Materials Research, Justus Liebig University Giessen, 35392 Giessen, Germany*; Email: erdogan.celik@materialwiss.uni giessen.de

Matthias T. Elm − *Center for Materials Research, Justus Liebig University Giessen, 35392 Giessen, Germany; Institute of Physical Chemistry, Justus Liebig University Giessen, 35392 Giessen, Germany; Institute of Experimental Physics I, Justus Liebig University Giessen, 35392 Giessen, Germany;* orcid.org/0000 0001 7014 5772; Email: matthias.elm@phys.chemie.uni giessen.de

Authors

Pascal Cop − *Center for Materials Research, Justus Liebig University Giessen, 35392 Giessen, Germany; Institute of Physical Chemistry, Justus Liebig University Giessen, 35392 Giessen, Germany*

Rajendra S. Negi − *Center for Materials Research, Justus Liebig University Giessen, 35392 Giessen, Germany*

Andrey Mazilkin − *Institute of Nanotechnology, Karlsruhe Institute of Technology (KIT), 76344 Eggenstein Leopoldshafen, Germany*

Yanjiao Ma − *Institute of Nanotechnology, Karlsruhe Institute of Technology (KIT), 76344 Eggenstein Leopoldshafen, Germany;* orcid.org/0000 0002 4125 2867

Philip Klement − *Center for Materials Research, Justus Liebig University Giessen, 35392 Giessen, Germany; Institute of Experimental Physics I, Justus Liebig University Giessen, 35392 Giessen, Germany;* orcid.org/0000 0001 7044 713X

Jörg Schörmann − *Center for Materials Research, Justus Liebig University Giessen, 35392 Giessen, Germany; Institute of Experimental Physics I, Justus Liebig University Giessen, 35392 Giessen, Germany*

Sangam Chatterjee − *Center for Materials Research, Justus Liebig University Giessen, 35392 Giessen, Germany; Institute of Experimental Physics I, Justus Liebig University Giessen, 35392 Giessen, Germany;* orcid.org/0000 0002 0237 5880

Torsten Brezesinski − *Institute of Nanotechnology, Karlsruhe Institute of Technology (KIT), 76344 Eggenstein Leopoldshafen, Germany;* orcid.org/0000 0002 4336 263X

Notes

The authors declare no competing financial interest.

ACKNOWLEDGMENTS

Financial support by the German Research Foundation (to T.B., Grant No. BR 3499/5 1 and to M.T.E., Grant No. EL 863/3 1) is gratefully acknowledged. P.K., R.S.N., and M.T.E. acknowledge the German Federal Ministry of Education and Research for funding the NanoMatFutur Project NiKo (Grant 03XP0093). S.C. acknowledges financial support by the Heisenberg Program (Grant CH660/8). The authors acknowledge the support from the Karlsruhe Nano Micro Facility (KNMF, www.knmf.kit.edu), a Helmholtz research infrastructure at Karlsruhe Institute of Technology (KIT, www.kit.edu).

REFERENCES

(1) Walcarius, A. Mesoporous Materials and Electrochemistry. *Chem. Soc. Rev.* **2013**, *42* (9), 4098.

(2) Rolison, D. R. Catalytic Nanoarchitectures The Importance of Nothing and the Unimportance of Periodicity. *Science* **2003**, *299* (5613), 1698−1701.

(3) Celik, E.; Ma, Y.; Brezesinski, T.; Elm, M. T. Ordered Mesoporous Metal Oxides for Electrochemical Applications: Correlation between Structure, Electrical Properties and Device Performance. *Phys. Chem. Chem. Phys.* **2021**, *23* (18), 10706−10735.

(4) Li, W.; Liu, J.; Zhao, D. Mesoporous Materials for Energy Conversion and Storage Devices. *Nat. Rev. Mater.* **2016**, *1* (6), 16023.

(5) Zu, L.; Zhang, W.; Qu, L.; Liu, L.; Li, W.; Yu, A.; Zhao, D. Mesoporous Materials for Electrochemical Energy Storage and Conversion. *Adv. Energy Mater.* **2020**, *10* (38), 2002152.

(6) Ren, Y.; Ma, Z.; Bruce, P. G. Ordered Mesoporous Metal Oxides: Synthesis and Applications. *Chem. Soc. Rev.* **2012**, *41* (14), 4909−4927.

(7) Liu, H.; Wang, G.; Liu, J.; Qiao, S.; Ahn, H. Highly Ordered Mesoporous NiO Anode Material for Lithium Ion Batteries with an Excellent Electrochemical Performance. *J. Mater. Chem.* **2011**, *21* (9), 3046−3052.

(8) Wagner, T.; Haffer, S.; Weinberger, C.; Klaus, D.; Tiemann, M. Mesoporous Materials as Gas Sensors. *Chem. Soc. Rev.* **2013**, *42* (9), 4036−4053.

(9) Baiutti, F.; Blanco Portals, J.; Anelli, S.; Torruella, P.; López Haro, M.; Calvino, J.; Estradé, S.; Torrell, M.; Peiró, F.; Tarancón, A. Tailoring the Transport Properties of Mesoporous Doped Cerium Oxide for Energy Applications. *J. Phys. Chem. C* **2021**, *125* (30), 16451−16463.

(10) Cherevan, A. S.; Deilmann, L.; Weller, T.; Eder, D.; Marschall, R. Mesoporous Semiconductors: A New Model To Assess Accessible

Surface Area and Increased Photocatalytic Activity? *ACS Appl. Energy Mater.* **2018**, *1* (11), 5787−5799.
(11) Brezesinski, T.; Wang, J.; Tolbert, S. H.; Dunn, B. Ordered Mesoporous α MoO_3 with Iso Oriented Nanocrystalline Walls for Thin Film Pseudocapacitors. *Nat. Mater.* **2010**, *9* (2), 146−151.
(12) Ren, Y.; Ma, Z.; Qian, L.; Dai, S.; He, H.; Bruce, P. G. Ordered Crystalline Mesoporous Oxides as Catalysts for CO Oxidation. *Catal. Lett.* **2009**, *131* (1−2), 146−154.
(13) Hartmann, P.; Lee, D. K.; Smarsly, B. M.; Janek, J. Mesoporous TiO_2: Comparison of Classical Sol−Gel and Nanoparticle Based Photoelectrodes for the Water Splitting Reaction. *ACS Nano* **2010**, *4* (6), 3147−3154.
(14) Kirchberg, K.; Wang, S.; Wang, L.; Marschall, R. Mesoporous $ZnFe_2O_4$ Photoanodes with Template Tailored Mesopores and Temperature Dependent Photocurrents. *ChemPhysChem* **2018**, *19* (18), 2313−2320.
(15) Weller, T.; Sann, J.; Marschall, R. Pore Structure Controlling the Activity of Mesoporous Crystalline $CsTaWO_6$ for Photocatalytic Hydrogen Generation. *Adv. Energy Mater.* **2016**, *6* (16), 1600208.
(16) Tiemann, M.; Weinberger, C. Selective Modification of Hierarchical Pores and Surfaces in Nanoporous Materials. *Adv. Mater. Interfaces* **2021**, *8* (4), 2001153.
(17) Bastakoti, B. P.; Kuila, D.; Salomon, C.; Konarova, M.; Eguchi, M.; Na, J.; Yamauchi, Y. Metal Incorporated Mesoporous Oxides: Synthesis and Applications. *J. Hazard. Mater.* **2021**, *401*, 123348.
(18) An, K.; Alayoglu, S.; Musselwhite, N.; Plamthottam, S.; Melaet, G.; Lindeman, A. E.; Somorjai, G. A. Enhanced CO Oxidation Rates at the Interface of Mesoporous Oxides and Pt Nanoparticles. *J. Am. Chem. Soc.* **2013**, *135* (44), 16689−16696.
(19) Tanaka, S.; Lin, J.; Kaneti, Y. V.; Yusa, S.; Jikihara, Y.; Nakayama, T.; Zakaria, M. B.; Alshehri, A. A.; You, J.; Hossain, M. S. A.; et al. Gold Nanoparticles Supported on Mesoporous Iron Oxide for Enhanced CO Oxidation Reaction. *Nanoscale* **2018**, *10* (10), 4779−4785.
(20) George, S. M. Atomic Layer Deposition: An Overview. *Chem. Rev.* **2010**, *110* (1), 111−131.
(21) Detavernier, C.; Dendooven, J.; Pulinthanathu Sree, S.; Ludwig, K. F.; Martens, J. A. Tailoring Nanoporous Materials by Atomic Layer Deposition. *Chem. Soc. Rev.* **2011**, *40* (11), 5242−5253.
(22) Asundi, A. S.; Raiford, J. A.; Bent, S. F. Opportunities for Atomic Layer Deposition in Emerging Energy Technologies. *ACS Energy Lett.* **2019**, *4* (4), 908−925.
(23) Zscherp, M. F.; Glaser, J.; Becker, C.; Beyer, A.; Cop, P.; Schörmann, J.; Volz, K.; Elm, M. T. Epitaxial Growth and Structural Characterization of Ceria Deposited by Atomic Layer Deposition on High Surface Porous Yttria Stabilized Zirconia Thin Films. *Cryst. Growth Des.* **2020**, *20* (4), 2194−2201.
(24) Elam, J. W.; Xiong, G.; Han, C. Y.; Wang, H. H.; Birrell, J. P.; Hryn, J. N.; Pellin, M. J.; Poco, J. F.; Satcher, J. H. Atomic Layer Deposition for the Conformal Coating of Nanoporous Materials. *MRS Proc.* **2005**, *876*, 126.
(25) Shin, J. W.; Go, D.; Kye, S. H.; Lee, S.; An, J. Review on Process Microstructure Performance Relationship in ALD Engineered SOFCs. *J. Phys. Energy* **2019**, *1* (4), 042002.
(26) Wen, L.; Zhou, M.; Wang, C.; Mi, Y.; Lei, Y. Nanoengineering Energy Conversion and Storage Devices via Atomic Layer Deposition. *Adv. Energy Mater.* **2016**, *6* (23), 1600468.
(27) Marichy, C.; Bechelany, M.; Pinna, N. Atomic Layer Deposition of Nanostructured Materials for Energy and Environ mental Applications. *Adv. Mater.* **2012**, *24* (8), 1017−1032.
(28) Kraffert, K.; Karg, M.; Schmack, R.; Clavel, G.; Boissiere, C.; Wirth, T.; Pinna, N.; Kraehnert, R. Stabilization of Mesoporous Iron Oxide Films against Sintering and Phase Transformations via Atomic Layer Deposition of Alumina and Silica. *Adv. Mater. Interfaces* **2018**, *5* (14), 1800360.
(29) Dubraja, L. A.; Boll, D.; Reitz, C.; Wang, D.; Belić, D.; Mazilkin, A.; Breitung, B.; Hahn, H.; Elm, M. T.; Brezesinski, T. Thin Films of Thermally Stable Ordered Mesoporous Rh_2O_3(I) for Visible Light Photocatalysis and Humidity Sensing. *ACS Appl. Nano Mater.* **2019**, *2* (11), 7126−7133.
(30) Pagán Torres, Y. J.; Gallo, J. M. R.; Wang, D.; Pham, H. N.; Libera, J. A.; Marshall, C. L.; Elam, J. W.; Datye, A. K.; Dumesic, J. A. Synthesis of Highly Ordered Hydrothermally Stable Mesoporous Niobia Catalysts by Atomic Layer Deposition. *ACS Catal.* **2011**, *1* (10), 1234−1245.
(31) Negi, R. S.; Culver, S. P.; Wiche, M.; Ahmed, S.; Volz, K.; Elm, M. T. Optimized Atomic Layer Deposition of Homogeneous, Conductive Al_2O_3 Coatings for High Nickel NCM Containing Ready to Use Electrodes. *Phys. Chem. Chem. Phys.* **2021**, *23* (11), 6725−6737.
(32) Hemmelmann, H.; Dinter, J. K.; Elm, M. T. Thin Film NCM Cathodes as Model Systems to Assess the Influence of Coating Layers on the Electrochemical Performance of Lithium Ion Batteries. *Adv. Mater. Interfaces* **2021**, *8* (9), 2002074.
(33) Neudeck, S.; Mazilkin, A.; Reitz, C.; Hartmann, P.; Janek, J.; Brezesinski, T. Effect of Low Temperature Al_2O_3 ALD Coating on Ni Rich Layered Oxide Composite Cathode on the Long Term Cycling Performance of Lithium Ion Batteries. *Sci. Rep.* **2019**, *9* (1), 5328.
(34) Kitsche, D.; Tang, Y.; Ma, Y.; Goonetilleke, D.; Sann, J.; Walther, F.; Bianchini, M.; Janek, J.; Brezesinski, T. High Performance All Solid State Batteries with a Ni Rich NCM Cathode Coated by Atomic Layer Deposition and Lithium Thiophosphate Solid Electro lyte. *ACS Appl. Energy Mater.* **2021**, *4* (7), 7338−7345.
(35) Meng, X.; Yang, X. Q.; Sun, X. Emerging Applications of Atomic Layer Deposition for Lithium Ion Battery Studies. *Adv. Mater.* **2012**, *24* (27), 3589−3615.
(36) Woo, J. H.; Trevey, J. E.; Cavanagh, A. S.; Choi, Y. S.; Kim, S. C.; George, S. M.; Oh, K. H.; Lee, S. H. Nanoscale Interface Modification of $LiCoO_2$ by Al_2O_3 Atomic Layer Deposition for Solid State Li Batteries. *J. Electrochem. Soc.* **2012**, *159* (7), A1120−A1124.
(37) Weber, D.; Tripković, D.; Kretschmer, K.; Bianchini, M.; Brezesinski, T. Surface Modification Strategies for Improving the Cycling Performance of Ni Rich Cathode Materials. *Eur. J. Inorg. Chem.* **2020**, *2020* (33), 3117−3130.
(38) Fan, Z.; Prinz, F. B. Enhancing Oxide Ion Incorporation Kinetics by Nanoscale Yttria Doped Ceria Interlayers. *Nano Lett.* **2011**, *11* (6), 2202−2205.
(39) Fan, Z.; Chao, C. C.; Hossein Babaei, F.; Prinz, F. B. Improving Solid Oxide Fuel Cells with Yttria Doped Ceria Interlayers by Atomic Layer Deposition. *J. Mater. Chem.* **2011**, *21* (29), 10903−10906.
(40) Chen, Y.; Gerdes, K.; Song, X. Nanoionics and Nanocatalysts: Conformal Mesoporous Surface Scaffold for Cathode of Solid Oxide Fuel Cells. *Sci. Rep.* **2016**, *6* (1), 32997.
(41) Tuller, H. L. Oxygen Ion Conduction and Structural Disorder in Conductive Oxides. *J. Phys. Chem. Solids* **1994**, *55* (12), 1393−1404.
(42) Fu, L.; Chen, C. C.; Maier, J. Interfacial Mass Storage in Nanocomposites. *Solid State Ionics* **2018**, *318*, 54−59.
(43) Chen, C. C.; Maier, J. Decoupling Electron and Ion Storage and the Path from Interfacial Storage to Artificial Electrodes. *Nat. Energy* **2018**, *3* (2), 102−108.
(44) Chen, C. C.; Fu, L.; Maier, J. Synergistic, Ultrafast Mass Storage and Removal in Artificial Mixed Conductors. *Nature* **2016**, *536* (7615), 159−164.
(45) Fu, L.; Tang, K.; Oh, H.; Manickam, K.; Bräuniger, T.; Chandran, C. V.; Menzel, A.; Hirscher, M.; Samuelis, D.; Maier, J. "Job Sharing" Storage of Hydrogen in Ru/Li_2O Nanocomposites. *Nano Lett.* **2015**, *15* (6), 4170−4175.
(46) Liao, P.; MacDonald, B. L.; Dunlap, R. A.; Dahn, J. R. Combinatorially Prepared $LiF_{1-x}Fe_x$ Nanocomposites for Positive Electrode Materials in Li Ion Batteries. *Chem. Mater.* **2008**, *20* (2), 454−461.
(47) Yu, X. Q.; Sun, J. P.; Tang, K.; Li, H.; Huang, X. J.; Dupont, L.; Maier, J. Reversible Lithium Storage in LiF/Ti Nanocomposites. *Phys. Chem. Chem. Phys.* **2009**, *11* (41), 9497−9503.

(48) Li, Q.; Li, H.; Xia, Q.; Hu, Z.; Zhu, Y.; Yan, S.; Ge, C.; Zhang, Q.; Wang, X.; Shang, X.; et al. Extra Storage Capacity in Transition Metal Oxide Lithium Ion Batteries Revealed by in Situ Magneto metry. *Nat. Mater.* **2021**, *20* (1), 76−83.
(49) Celik, E.; Negi, R. S.; Bastianello, M.; Boll, D.; Mazilkin, A.; Brezesinski, T.; Elm, M. T. Tailoring the Protonic Conductivity of Porous Yttria Stabilized Zirconia Thin Films by Surface Modification. *Phys. Chem. Chem. Phys.* **2020**, *22* (20), 11519−11528.
(50) Cop, P.; Celik, E.; Hess, K.; Moryson, Y.; Klement, P.; Elm, M. T.; Smarsly, B. M. Atomic Layer Deposition of Nanometer Sized CeO_2 Layers in Ordered Mesoporous ZrO_2 Films and Their Impact on the Ionic/Electronic Conductivity. *ACS Appl. Nano Mater.* **2020**, *3* (11), 10757−10766.
(51) Jacobson, A. J. Materials for Solid Oxide Fuel Cells. *Chem. Mater.* **2010**, *22* (3), 660−674.
(52) Hui, S.; Roller, J.; Yick, S.; Zhang, X.; Decès Petit, C.; Xie, Y.; Maric, R.; Ghosh, D. A Brief Review of the Ionic Conductivity Enhancement for Selected Oxide Electrolytes. *J. Power Sources* **2007**, *172* (2), 493−502.
(53) Kilner, J. A.; Burriel, M. Materials for Intermediate Temper ature Solid Oxide Fuel Cells. *Annu. Rev. Mater. Res.* **2014**, *44* (1), 365−393.
(54) Elm, M. T.; Hofmann, J. D.; Suchomski, C.; Janek, J.; Brezesinski, T. Ionic Conductivity of Mesostructured Yttria Stabilized Zirconia Thin Films with Cubic Pore Symmetry—On the Influence of Water on the Surface Oxygen Ion Transport. *ACS Appl. Mater. Interfaces* **2015**, *7* (22), 11792−11801.
(55) Park, J.; Blumenthal, R. N. Electronic Transport in 8 Mole Percent Y_2O_3 ZrO_2. *J. Electrochem. Soc.* **1989**, *136* (10), 2867−2876.
(56) Trovarelli, A. Catalytic Properties of Ceria and CeO_2 Containing Materials. *Catal. Rev.* **1996**, *38* (4), 439−520.
(57) Michel, K.; Eufinger, J. P.; Ulbrich, G.; Lerch, M.; Janek, J.; Elm, M. T. Combining Two Redox Active Rare Earth Elements for Oxygen Storage − Electrical Properties and Defect Chemistry of Ceria−Praseodymia Single Crystals. *Phys. Chem. Chem. Phys.* **2017**, *19* (27), 17661−17669.
(58) Tuller, H. L.; Nowick, A. S. Small Polaron Electron Transport in Reduced CeO_2 Single Crystals. *J. Phys. Chem. Solids* **1977**, *38* (8), 859−867.
(59) Tuller, H. L.; Nowick, A. S. Defect Structure and Electrical Properties of Nonstoichiometric CeO_2 Single Crystals. *J. Electrochem. Soc.* **1979**, *126* (2), 209−217.
(60) Naik, I. K.; Tien, T. Y. Small Polaron Mobility in Non stoichiometric Cerium Dioxide. *J. Phys. Chem. Solids* **1978**, *39* (3), 311−315.
(61) Chiang, Y. M.; Lavik, E. B.; Kosacki, I.; Tuller, H. L.; Ying, J. Y. Nonstoichiometry and Electrical Conductivity of Nanocrystalline CeO_{2-x}. *J. Electroceramics* **1997**, *1* (1), 7−14.
(62) Yashima, M.; Sasaki, S.; Kakihana, M.; Yamaguchi, Y.; Arashi, H.; Yoshimura, M. Oxygen Induced Structural Change of the Tetragonal Phase around the Tetragonal−Cubic Phase Boundary in ZrO_2−$YO_{1.5}$ Solid Solutions. *Acta Crystallogr. Sect. B Struct. Sci.* **1994**, *50* (6), 663−672.
(63) Debye, P.; Scherrer, P. Atombau. *Nachrichten von der Gesellschaft der Wissenschaften zu Göttingen, Math. Klasse* **1918**, *1918*, 101−120.
(64) Fujimori, H.; Yashima, M.; Sasaki, S.; Kakihana, M.; Mori, T.; Tanaka, M.; Yoshimura, M. Internal Distortion in Ceria Doped Hafnia Solid Solutions: High Resolution X Ray Diffraction and Raman Scattering. *Phys. Rev. B* **2001**, *64* (13), 134104.
(65) Sun, Y.; Li, C.; Djerdj, I.; Khalid, O.; Cop, P.; Sann, J.; Weber, T.; Werner, S.; Turke, K.; Guo, Y.; et al. Oxygen Storage Capacity versus Catalytic Activity of Ceria−Zirconia Solid Solutions in CO and HCl Oxidation. *Catal. Sci. Technol.* **2019**, *9* (9), 2163−2172.
(66) Briois, P.; Lapostolle, F.; Demange, V.; Djurado, E.; Billard, A. Structural Investigations of YSZ Coatings Prepared by DC Magnetron Sputtering. *Surf. Coat. Technol.* **2007**, *201* (12), 6012−6018.
(67) Cai, J.; Raptis, C.; Raptis, Y. S.; Anastassakis, E. Temperature Dependence of Raman Scattering in Stabilized Cubic Zirconia. *Phys. Rev. B* **1995**, *51* (1), 201−209.
(68) Popović, Z. V.; Dohčević Mitrović, Z.; Šćepanović, M.; Grujić Brojčin, M.; Aškrabić, S. Raman Scattering on Nanomaterials and Nanostructures. *Ann. Phys.* **2011**, *523* (1−2), 62−74.
(69) Chan, C. K.; Peng, H.; Liu, G.; McIlwrath, K.; Zhang, X. F.; Huggins, R. A.; Cui, Y. High Performance Lithium Battery Anodes Using Silicon Nanowires. *Nat. Nanotechnol.* **2008**, *3* (1), 31−35.
(70) Kosacki, I.; Suzuki, T.; Anderson, H. U.; Colomban, P. Raman Scattering and Lattice Defects in Nanocrystalline CeO_2 Thin Films. *Solid State Ionics* **2002**, *149* (1−2), 99−105.
(71) Kourouklis, G. A.; Jayaraman, A.; Espinosa, G. P. High Pressure Raman Study of CeO_2 to 35 GPa and Pressure Induced Phase Transformation from the Fluorite Structure. *Phys. Rev. B* **1988**, *37* (8), 4250−4253.
(72) Spanier, J. E.; Robinson, R. D.; Zhang, F.; Chan, S. W.; Herman, I. P. Size Dependent Properties of CeO_{2-y} Nanoparticles as Studied by Raman Scattering. *Phys. Rev. B* **2001**, *64* (24), 245407.
(73) Campbell, I. H.; Fauchet, P. M. The Effects of Microcrystal Size and Shape on the One Phonon Raman Spectra of Crystalline Semiconductors. *Solid State Commun.* **1986**, *58* (10), 739−741.
(74) Filtschew, A.; Hofmann, K.; Hess, C. Ceria and Its Defect Structure: New Insights from a Combined Spectroscopic Approach. *J. Phys. Chem. C* **2016**, *120* (12), 6694−6703.
(75) Dohčević Mitrović, Z. D.; Šćepanović, M. J.; Grujić Brojčin, M. U.; Popović, Z. V.; Bošković, S. B.; Matović, B. M.; Zinkevich, M. V.; Aldinger, F. The Size and Strain Effects on the Raman Spectra of $Ce_{1-x}Nd_xO_{2-\delta}$ ($0 \leq x \leq 0.25$) Nanopowders. *Solid State Commun.* **2006**, *137* (7), 387−390.
(76) Gupta, M.; Kumar, A.; Sagdeo, A.; Sagdeo, P. R. Doping Induced Combined Fano and Phonon Confinement Effect in La Doped CeO_2: Raman Spectroscopy Analysis. *J. Phys. Chem. C* **2021**, *125* (4), 2648−2658.
(77) Weber, W. H.; Hass, K. C.; McBride, J. R. Raman Study of CeO_2: Second Order Scattering, Lattice Dynamics, and Particle Size Effects. *Phys. Rev. B* **1993**, *48* (1), 178−185.
(78) Konetschny, A.; Weinhold, M.; Heiliger, C.; Elm, M. T.; Klar, P. J. Polarization Dependence of the Raman Response of Free Standing Strained $Ce_{0.8}Gd_{0.2}O_2$ Membranes. *Phys. Chem. Chem. Phys.* **2021**, *23* (11), 6903−6913.
(79) Dendooven, J.; Devloo Casier, K.; Ide, M.; Grandfield, K.; Kurttepeli, M.; Ludwig, K. F.; Bals, S.; Van Der Voort, P.; Detavernier, C. Atomic Layer Deposition Based Tuning of the Pore Size in Mesoporous Thin Films Studied by in Situ Grazing Incidence Small Angle X Ray Scattering. *Nanoscale* **2014**, *6* (24), 14991−14998.
(80) Ma, Y.; Ma, Y.; Giuli, G.; Euchner, H.; Groß, A.; Lepore, G. O.; D'Acapito, F.; Geiger, D.; Biskupek, J.; Kaiser, U.; et al. Introducing Highly Redox Active Atomic Centers into Insertion Type Electrodes for Lithium Ion Batteries. *Adv. Energy Mater.* **2020**, *10* (25), 2000783.
(81) Artiglia, L.; Agnoli, S.; Paganini, M. C.; Cattelan, M.; Granozzi, G. TiO_2@CeO_x Core Shell Nanoparticles as Artificial Enzymes with Peroxidase like Activity. *ACS Appl. Mater. Interfaces* **2014**, *6* (22), 20130−20136.
(82) Yue, J.; Suchomski, C.; Voepel, P.; Ellinghaus, R.; Rohnke, M.; Leichtweiss, T.; Elm, M. T.; Smarsly, B. M. Mesoporous Niobium Doped Titanium Dioxide Films from the Assembly of Crystalline Nanoparticles: Study on the Relationship between the Band Structure, Conductivity and Charge Storage Mechanism. *J. Mater. Chem. A* **2017**, *5* (5), 1978−1988.
(83) Hao, X.; Yoko, A.; Chen, C.; Inoue, K.; Saito, M.; Seong, G.; Takami, S.; Adschiri, T.; Ikuhara, Y. Atomic Scale Valence State Distribution inside Ultrafine CeO_2 Nanocubes and Its Size Depend ence. *Small* **2018**, *14* (42), 1802915.
(84) Hartmann, P.; Brezesinski, T.; Sann, J.; Lotnyk, A.; Eufinger, J. P.; Kienle, L.; Janek, J. Defect Chemistry of Oxide Nanomaterials with High Surface Area: Ordered Mesoporous Thin Films of the Oxygen Storage Catalyst CeO_2−ZrO_2. *ACS Nano* **2013**, *7* (4), 2999−3013.

(85) Sun, S.; Gao, Q.; Wang, H.; Zhu, J.; Guo, H. Influence of Textural Parameters on the Catalytic Behavior for CO Oxidation over Ordered Mesoporous Co_3O_4. *Appl. Catal. B Environ.* **2010**, *97* (1−2), 284−291.
(86) Fleig, J. The Grain Boundary Impedance of Random Microstructures: Numerical Simulations and Implications for the Analysis of Experimental Data. *Solid State Ionics* **2002**, *150* (1), 181−193.
(87) Irvine, J. T. S.; Sinclair, D. C.; West, A. R. Electroceramics: Characterization by Impedance Spectroscopy. *Adv. Mater.* **1990**, *2* (3), 132−138.
(88) Gerstl, M.; Navickas, E.; Friedbacher, G.; Kubel, F.; Ahrens, M.; Fleig, J. The Separation of Grain and Grain Boundary Impedance in Thin Yttria Stabilized Zirconia (YSZ) Layers. *Solid State Ionics* **2011**, *185* (1), 32−41.
(89) Kosacki, I.; Anderson, H. U. Microstructure — Property Relationships in Nanocrystalline Oxide Thin Films. *Ionics (Kiel).* **2000**, *6* (3), 294−311.
(90) Bieberle Hütter, A.; Hertz, J. L.; Tuller, H. L. Fabrication and Electrochemical Characterization of Planar Pt−CGO Microstructures. *Acta Mater.* **2008**, *56* (2), 177−187.
(91) Jiang, J.; Hertz, J. L. On the Variability of Reported Ionic Conductivity in Nanoscale YSZ. Thin Films. *J. Electroceramics* **2014**, *32* (1), 37−46.
(92) Eckhardt, J. K.; Burkhardt, S.; Zahnow, J.; Elm, M. T.; Janek, J.; Klar, P. J.; Heiliger, C. Understanding the Impact of Microstructure on Charge Transport in Polycrystalline Materials Through Impedance Modelling. *J. Electrochem. Soc.* **2021**, *168* (9), 090516.
(93) Zahnow, J.; Bernges, T.; Wagner, A.; Bohn, N.; Binder, J. R.; Zeier, W. G.; Elm, M. T.; Janek, J. Impedance Analysis of NCM Cathode Materials: Electronic and Ionic Partial Conductivities and the Influence of Microstructure. *ACS Appl. Energy Mater.* **2021**, *4* (2), 1335−1345.
(94) Kogut, I.; Steiner, C.; Wulfmeier, H.; Wollbrink, A.; Hagen, G.; Moos, R.; Fritze, H. Comparison of the Electrical Conductivity of Bulk and Film $Ce_{1-x}Zr_xO_{2-\delta}$ in Oxygen Depleted Atmospheres at High Temperatures. *J. Mater. Sci.* **2021**, *56* (30), 17191−17204.
(95) Chiodelli, G.; Flor, G.; Scagliotti, M. Electrical Properties of the ZrO_2 CeO_2 System. *Solid State Ionics* **1996**, *91* (1), 109−121.
(96) Huang, B.; Gillen, R.; Robertson, J. Study of CeO_2 and Its Native Defects by Density Functional Theory with Repulsive Potential. *J. Phys. Chem. C* **2014**, *118* (42), 24248−24256.
(97) Keating, P. R. L.; Scanlon, D. O.; Morgan, B. J.; Galea, N. M.; Watson, G. W. Analysis of Intrinsic Defects in CeO_2 Using a Koopmans Like GGA+ U Approach. *J. Phys. Chem. C* **2012**, *116* (3), 2443−2452.
(98) Zacherle, T.; Schriever, A.; De Souza, R. A.; Martin, M. Ab Initio Analysis of the Defect Structure of Ceria. *Phys. Rev. B Condens. Matter Mater. Phys.* **2013**, *87* (13), 134104.
(99) Neumeier, J. J.; Elm, M. T.; Luerßen, B.; Janek, J. Platinum Microelectrodes on Gadolinia Doped Ceria Single Crystals − Bulk Properties and Electrode Kinetics. *Phys. Chem. Chem. Phys.* **2018**, *20* (12), 8294−8301.
(100) Kosacki, I.; Suzuski, T.; Petrovsky, V.; Anderson, H. U. Electrical Conductivity of Nanocrystalline Ceria and Zirconia Thin Films. *Solid State Ionics* **2000**, *136−137* (1−2), 1225−1233.
(101) Tuller, H. L. Semiconduction and Mixed Ionic Electronic Conduction in Nonstoichiometric Oxides: Impact and Control. *Solid State Ionics* **1997**, *94* (1), 63−74.
(102) Chiang, Y. M.; Lavik, E. B.; Kosacki, I.; Tuller, H. L.; Ying, J. Y. Defect and Transport Properties of Nanocrystalline CeO_{2-x}. *Appl. Phys. Lett.* **1996**, *69* (2), 185−187.
(103) Tschöpe, A. Grain Size Dependent Electrical Conductivity of Polycrystalline Cerium Oxide. II: Space Charge Model. *Solid State Ionics* **2001**, *139* (3−4), 267−280.
(104) Migani, A.; Vayssilov, G. N.; Bromley, S. T.; Illas, F.; Neyman, K. M. Dramatic Reduction of the Oxygen Vacancy Formation Energy in Ceria Particles: A Possible Key to Their Remarkable Reactivity at the Nanoscale. *J. Mater. Chem.* **2010**, *20* (46), 10535−10546.
(105) Migani, A.; Vayssilov, G. N.; Bromley, S. T.; Illas, F.; Neyman, K. M. Greatly Facilitated Oxygen Vacancy Formation in Ceria Nanocrystallites. *Chem. Commun.* **2010**, *46* (32), 5936−5938.
(106) Marrocchelli, D.; Bishop, S. R.; Tuller, H. L.; Yildiz, B. Understanding Chemical Expansion in Non Stoichiometric Oxides: Ceria and Zirconia Case Studies. *Adv. Funct. Mater.* **2012**, *22* (9), 1958−1965.
(107) Weidmann, C.; Brezesinski, K.; Suchomski, C.; Tropp, K.; Grosser, N.; Haetge, J.; Smarsly, B. M.; Brezesinski, T. Morphology Controlled Synthesis of Nanocrystalline η Al_2O_3 Thin Films, Powders, Microbeads, and Nanofibers with Tunable Pore Sizes from Preformed Oligomeric Oxo Hydroxo Building Blocks. *Chem. Mater.* **2012**, *24* (3), 486−494.
(108) Reitz, C.; Haetge, J.; Suchomski, C.; Brezesinski, T. Facile and General Synthesis of Thermally Stable Ordered Mesoporous Rare Earth Oxide Ceramic Thin Films with Uniform Mid Size to Large Size Pores and Strong Crystalline Texture. *Chem. Mater.* **2013**, *25* (22), 4633−4642.
(109) Graberg, T. Von; Hartmann, P.; Rein, A.; Gross, S.; Seelandt, B.; Röger, C.; Zieba, R.; Traut, A.; Wark, M.; Janek, J.; et al. Mesoporous Tin Doped Indium Oxide Thin Films: Effect of Mesostructure on Electrical Conductivity. *Sci. Technol. Adv. Mater.* **2011**, *12* (2), 025005.
(110) Wang, Y.; Brezesinski, T.; Antonietti, M.; Smarsly, B. Ordered Mesoporous Sb , Nb , and Ta Doped SnO_2 Thin Films with Adjustable Doping Levels and High Electrical Conductivity. *ACS Nano* **2009**, *3* (6), 1373−1378.
(111) Brinker, C. J. Evaporation Induced Self Assembly: Functional Nanostructures Made Easy. *MRS Bull.* **2004**, *29* (9), 631−640.
(112) Crepaldi, E. L.; de A. A. Soler Illia, G. J.; Bouchara, A.; Grosso, D.; Durand, D.; Sanchez, C. Controlled Formation of Highly Ordered Cubic and Hexagonal Mesoporous Nanocrystalline Yttria−Zirconia and Ceria−Zirconia Thin Films Exhibiting High Thermal Stability. *Angew. Chemie Int. Ed.* **2003**, *42* (3), 347−351.
(113) Romeo, M.; Bak, K.; El Fallah, J.; Le Normand, F.; Hilaire, L. XPS Study of the Reduction of Cerium Dioxide. *Surf. Interface Anal.* **1993**, *20* (6), 508−512.
(114) Skála, T.; Šutara, F.; Prince, K. C.; Matolín, V. Cerium Oxide Stoichiometry Alteration via Sn Deposition: Influence of Temperature. *J. Electron Spectrosc. Relat. Phenom.* **2009**, *169* (1), 20−25.